MATERIALS SCIENCE

Understanding the asymmetrical thermoelectric performance for discovering promising thermoelectric materials

Hangtian Zhu[1]*, Jun Mao[1]*, Zhenzhen Feng[2,3,4], Jifeng Sun[2], Qing Zhu[1], Zihang Liu[1], David J. Singh[2†], Yumei Wang[5†], Zhifeng Ren[1†]

Thermoelectric modules, consisting of multiple pairs of n- and p-type legs, enable converting heat into electricity and vice versa. However, the thermoelectric performance is often asymmetrical, in that one type outperforms the other. In this paper, we identified the relationship between the asymmetrical thermoelectric performance and the weighted mobility ratio, a correlation that can help predict the thermoelectric performance of unreported materials. Here, a reasonably high *ZT* for the n-type ZrCoBi-based half-Heuslers is first predicted and then experimentally verified. A high peak *ZT* of ~1 at 973 K can be realized by $ZrCo_{0.9}Ni_{0.1}Bi_{0.85}Sb_{0.15}$. The measured heat-to-electricity conversion efficiency for the unicouple of ZrCoBi-based materials can be as high as ~10% at the cold-side temperature of ~303 K and at the hot-side temperature of ~983 K. Our work demonstrates that the ZrCoBi-based half-Heuslers are highly promising for the application of mid- and high-temperature thermoelectric power generation.

INTRODUCTION

Solid-state energy conversion from heat to electricity and vice versa can be realized by a thermoelectric module using a thermoelectric material (*1*, *2*). The conversion efficiency of the module is governed by the Carnot efficiency and by the material's figure of merit (*ZT*). $ZT = [S^2\sigma/(\kappa_L + \kappa_e)]T$, where S, σ, κ_L, κ_e, and T are the Seebeck coefficient, electrical conductivity, lattice thermal conductivity, electronic thermal conductivity, and absolute temperature, respectively (*3*). Generally, the thermoelectric module consists of multiple pairs of n- and p-type legs that are connected thermally in parallel and electrically in series (*4*). To achieve a high-energy conversion efficiency, high thermoelectric performance for both types of legs is desired. In addition, to minimize the thermal stress that originates from the mismatch of thermal expansion coefficients between n- and p-type legs, it is preferable to adopt the same base compound for both types of legs.

However, there are quite a few materials that can only be synthesized as one of the types, e.g., MgAgSb (*5*–*7*), SnTe (*8*, *9*), GeTe (*10*–*12*), and Zn_4Sb_3 (*13*). This can be attributed to the presence of native defects that pin the Fermi level to either the conduction or the valence band, and therefore, the materials show persistent n- or p-type conduction (*14*). Among the materials for which the ambipolar doping can be realized, most show high thermoelectric performance (i.e., $ZT > 1$) in only one of the types: e.g., Mg_2Sn-based (*15*–*18*), Mg_3Sb_2-based (*19*–*22*), ZrNiSn-based (*23*, *24*), and NbFeSb-based (*25*–*27*) compounds. Even for the state-of-the-art thermoelectric materials, e.g., Bi_2Te_3-based materials (*28*, *29*), lead chalcogenides (*30*–*35*), skutterudites (*36*, *37*), and SiGe (*38*, *39*), in which high thermoelectric performance can be achieved in both types, the thermoelectric performance is often asymmetrical (Fig. 1). The specific reason for such an asymmetry varies among the different compounds. It could be attributed to the difference in the electronic structures between the conduction and valence bands, e.g., density-of-state effective mass (m_d^*), inertial effective mass (m_I), and band degeneracy (N). It can also be ascribed to the difference in carrier mobility due to the different degree of carrier scattering (*33*). In addition, disparity in the dopability, e.g., difficulty in identifying an efficient dopant for one of the types, can also lead to asymmetrical thermoelectric performance.

The asymmetrical thermoelectric performance of previously reported materials has been merely viewed as an observation, while a more general relationship between the asymmetry and intrinsic material parameters is seldom discussed. Therefore, it would be highly meaningful to quantify the asymmetrical thermoelectric performance and identify the relationship between the asymmetry and the materials' parameters. This would be highly beneficial for understanding the asymmetrical thermoelectric performance. Once the relationship can be identified, it would be possible to predict the thermoelectric performance of an unreported type of a given material by using the material's intrinsic parameters. Such a strategy could possibly be helpful for identifying promising thermoelectric materials.

RESULTS

Asymmetrical thermoelectric performance and materials' parameters

Generally, the lattice thermal conductivity of optimized p- and n-type compositions of a given material system are similar. Therefore, we mainly focus on the electronic transport properties of the materials. The electronic contributions to thermoelectric performance are given by a power factor, which can be optimized by chemical doping. The thermoelectric performance of a given compound can be estimated by the dimensionless material quality factor B (*40*, *41*)

$$B = 5.745 \times 10^{-6} \frac{\mu (m_d^*)^{3/2}}{\kappa_L} T^{5/2} \quad (1)$$

[1]Department of Physics and Texas Center for Superconductivity, University of Houston, Houston, TX 77204, USA. [2]Department of Physics and Astronomy, University of Missouri, Columbia, MO 65211, USA. [3]Key Laboratory of Materials Physics, Institute of Solid State Physics, Chinese Academy of Sciences, Hefei 230031, China. [4]Science Island Branch of the Graduate School, University of Science and Technology of China, Hefei 230026, China. [5]Beijing National Laboratory for Condensed Matter Physics, Institute of Physics, Chinese Academy of Sciences, P.O. Box 603, Beijing 100190, China.
*These authors contributed equally to this work.
†Corresponding author. Email: singhdj@missouri.edu (D.J.S.); wangym@iphy.ac.cn (Y.W.); zren@uh.edu (Z.R.)

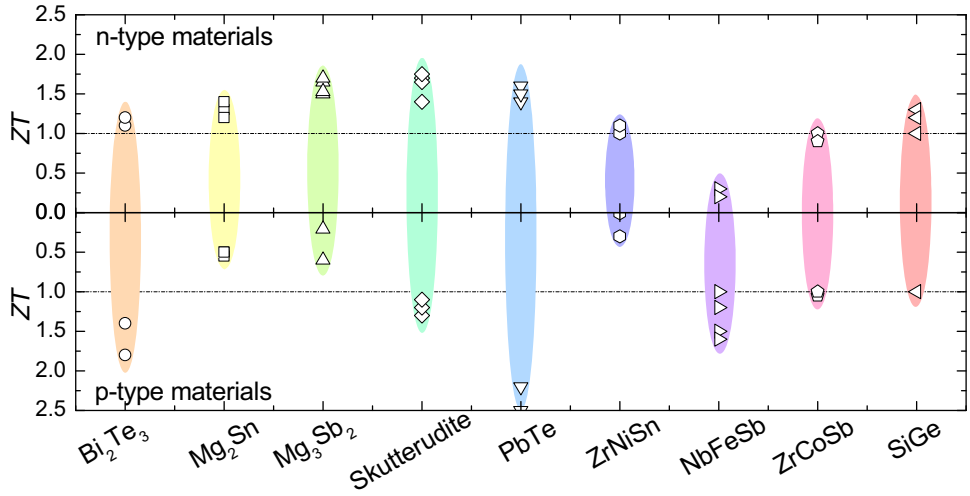

Fig. 1. Dimensionless figure of merit for a series of thermoelectric materials (also including their solid solutions) with n- and p-type conduction.

where μ is the carrier mobility. This formula captures the essential aspect that heavy effective mass (for the thermopower), high carrier mobility (which typically accompanies light mass and is needed for conductivity), and low lattice thermal conductivity are all needed for thermoelectric performance. When asymmetrical thermoelectric performance is observed for a certain compound, this asymmetry (n-type versus p-type) can then be estimated by

$$\frac{B_n}{B_p} = \frac{5.745 \times 10^{-6} \frac{\mu_n (m^*_{d,n})^{3/2}}{\kappa_{L,n}} T_n^{5/2}}{5.745 \times 10^{-6} \frac{\mu_p (m^*_{d,p})^{3/2}}{\kappa_{L,p}} T_p^{5/2}} \approx \frac{\mu_n (m^*_{d,n})^{3/2}}{\mu_p (m^*_{d,p})^{3/2}} = A \quad (2)$$

where n denotes the n-type and p denotes the p-type. κ_L and the temperature for peak ZT are considered similar for both n- and p-types of the compound. A is the dimensionless n-type to p-type weighted mobility ratio. The density-of-state effective mass is related to the band effective mass (m_b) via the relation of $m^*_d = N^{2/3} m_b$. In addition, in the case when carriers are mainly scattered by acoustic phonons, the carrier mobility depends on the band effective mass as well as the inertial effective mass according to the relation of $\mu \propto m_I^{-1} m_b^{-3/2}$. For an isotropic single parabolic band system, these masses are identical, and in the general case, they are decoupled and are also dependent on doping and temperature. Equation 2 can thus be rewritten as

$$A \approx \frac{N_n m_{I,p}}{N_p m_{I,n}} \quad (3)$$

It can be understood from Eq. 3 that a large band degeneracy (*30*) and a low inertial effective mass (*32*) will be greatly beneficial for high thermoelectric performance. As a result, the difference in the band degeneracy and inertial effective mass between the conduction and valence bands will lead to a noticeable asymmetrical thermoelectric performance. According to Eq. 2, the asymmetrical thermoelectric performance can be estimated by the weighted mobility ratio. The weighted mobility ratio for different materials could, in principle, be calculated by Eq. 2. For estimation of A, this can be done at similar electron and hole carrier concentration. The relationship between the n-type to p-type ZT ratio (ZT_n/ZT_p) and the n-type to p-type weighted mobility ratio is shown in Fig. 2A. There is a general trend that ZT_n/ZT_p increases with the weighted mobility ratio, i.e., $\log(ZT_n/ZT_p) = C_1 \log(A) + C_2$, where C_1 and C_2 are fitted as 0.69 and −0.039, respectively. Details of the data used in this fitting can be found in table S1. It should be noted that the experimentally obtained relationship between $\log(ZT_n/ZT_p)$ and $\log(A)$ is in a reasonably good agreement with the theoretical calculation (section S1 and fig. S1). Specifically, when the weighted mobility ratio is larger than unity, the n-type material will outperform the p-type counterpart ($ZT_n/ZT_p > 1$). Conversely, when the weighted mobility ratio is smaller than unity, the p-type compound will demonstrate better thermoelectric performance ($ZT_n/ZT_p < 1$). When the thermoelectric performance for one type of a material has been experimentally studied, while the other type has not yet been investigated, it is possible to predict the ZT by using the identified relationship between the asymmetry and weighted mobility ratio. In this case, because the carrier mobility for the unreported type cannot be obtained, Eq. 3 can be adopted to estimate the weighted mobility ratio as it only involves the material's basic parameters that can be determined by calculation. However, it should be noted that Eq. 3 is simplified by assuming that the carrier scattering is similar for electrons (n-type specimen) and holes (p-type specimen). Therefore, the estimated weighted mobility ratio by Eq. 3 could be different from the value experimentally determined by Eq. 2. Here, we have predicted the thermoelectric performance for several materials as shown in Fig. 2B. Our predictions indicate that reasonably high ZT can possibly be achieved in n-type SnTe, n-type GeTe, and n-type ZrCoBi. In addition, n-type TaFeSb and p-type NbCoSn are possible candidates for very promising thermoelectric performance. However, SnTe and GeTe have been proven as very persistent p-type materials, so we limited our investigation to the thermoelectric properties of the half-Heusler materials. Currently, we have not yet identified efficient dopants for p-type NbCoSn or n-type TaFeSb (fig. S2). Therefore, we will mainly discuss the thermoelectric properties of n-type ZrCoBi-based materials in this work.

Electronic structure of ZrCoBi

Theoretical calculations of the electronic structure of ZrCoBi were first conducted to provide preliminary insight into its thermoelectric

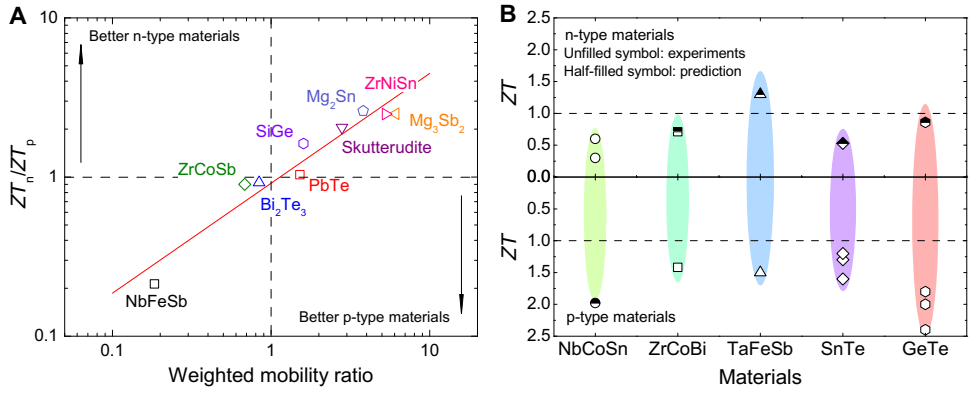

Fig. 2. Relationship between the asymmetrical thermoelectric performance and weighted mobility ratio. (**A**) Relationship between the *ZT* ratio (n-type versus p-type) and weighted mobility ratio. (**B**) Predicted thermoelectric performance for a number of materials.

performance. The calculated band structure of ZrCoBi is shown in Fig. 3A. The valence bands show practically degenerate maxima at Γ and L, which is a previously discussed band convergence (*42*). It should be noted that there are strong splittings in the bands as one moves away from Γ. These are the splitting into a heavy- and light-hole band along Γ-X and an additional splitting of the upper heavy-hole band along Γ-L. This latter splitting would be forbidden without the combination of spin-orbit and non-centrosymmetry. These effects are strong due to the large difference between Co, Zr and the heavy p-electron element Bi, which leads to strong breaking parity symmetry, *P*. Although Γ has the full cubic symmetry, and the inverse effective mass tensor of a cubic material is isotropic, the bands at Γ are evidently highly anisotropic. This anisotropy with different curvatures in different bands and directions at Γ provides a mechanism for decoupling the electrical conductivity and the Seebeck coefficient, in particular with the high curvature areas, leading to high electrical conductivity. Even more notably, at the other pocket L, there is a pair of two-fold degenerate bands separated by 0.06 eV. Both are relevant for the thermoelectric transport due to this small splitting. The upper band is seen to be very strongly spin-split from L to W and somewhat more weakly so along L-Γ. This splitting would be forbidden by the combination of parity and time reversal in a centrosymmetric case. This is important because, in addition to the anisotropy allowed in a parabolic system around the L point [i.e., a transverse and a longitudinal mass, which can be different, as in GeTe (*43*)], there is an additional separation into a light and heavy band due to spin-orbit. This is highly favorable as it again decouples Seebeck coefficient and electrical conductivity. In contrast, the conduction band structure is apparently simpler, although it also shows strong influence of spin-orbit. This band shows a substantial spin-splitting along X-W but not X-Γ. This Dresselhaus spin-splitting shifts the conduction band minimum away from X perpendicular to the X-Γ line and can also decouple the Seebeck coefficient and electrical conductivity, although the decoupling is less pronounced than in the valence bands.

Visualization of the carrier pockets 0.1 eV from the band edges for the p- and n-type ZrCoBi are shown in Fig. 3 (C and D). The band degeneracy (*N*) is 10 for the p-type ZrCoBi but only 3 for its n-type counterpart. In addition, the calculated inertial effective mass is shown as a function of carrier concentration for n- and p-type ZrCoBi in Fig. 3B. It should be noted that the inertial effective mass (m_I) is very similar for n- and p-type ZrCoBi. As a result, the value of N/m_I is ~5.3 m_0^{-1} for p-type ZrCoBi and only ~2.2 m_0^{-1} for its n-type counterpart, which corresponds to an n-type to p-type weighted mobility ratio of ~0.42. By using the experimentally determined thermoelectric performance of p-type ZrCoBi-based materials (i.e., peak *ZT* of ~1.4) and the weighted mobility ratio of ~0.42, the predicted *ZT* for n-type ZrCoBi is about ~0.71 (Fig. 2B). That is, despite the asymmetrical thermoelectric performance of ZrCoBi (i.e., the p-type outperforming the n-type), reasonably high thermoelectric performance could possibly be achieved in the n-type ZrCoBi.

Electronic properties of n-type ZrCoBi

The n-type Ni-doped ZrCoBi-based materials were prepared by the ball-milling and hot-pressing method. All the samples are single phase (fig. S3) and highly dense (fig. S4). The measured electronic properties of the n-type ZrCoBi-based half-Heuslers are shown in Fig. 4. The undoped ZrCoBi shows a low electrical conductivity, and after Ni doping at the Co site, the electrical conductivity is substantially improved (Fig. 4A). Such an enhancement should be mainly attributed to the increased Hall carrier concentration. As shown in fig. S5, the carrier concentration increases monotonically with the Ni concentration. This indicates that Ni is an efficient dopant for supplying electrons to ZrCoBi, similar to the case of ZrCoSb (*44*). Accordingly, the Seebeck coefficient of $ZrCo_{1-x}Ni_xBi$ decreases with the increase of Ni concentration (Fig. 4B), with the exception of the undoped ZrCoBi. By optimizing the carrier concentration, a reasonably high peak power factor ($S^2\sigma$) of ~27 μW cm^{-1} K^{-2} can be realized by $ZrCo_{0.9}Ni_{0.1}Bi$ (Fig. 4C). The power factor of p-type $ZrCoBi_{0.8}Sn_{0.2}$ is also plotted for comparison (black solid line), and it is noticeably higher than that of the n-type specimens over the whole temperature range. The average power factor between 300 and 973 K can be calculated by the integration method, and it is ~20.8 μW cm^{-1} K^{-2} for n-type $ZrCo_{0.9}Ni_{0.1}Bi$ and as high as ~33.6 μW cm^{-1} K^{-2} for p-type $ZrCoBi_{0.8}Sn_{0.2}$. Such a marked difference in the power factor between the n- and p-type ZrCoBi-based materials should be mainly ascribed to the difference in band degeneracy and pocket shape between the conduction and valence bands. Therefore, despite the similar inertial effective mass between the n- and p-type ZrCoBi, the density-of-state effective masses of p-type ZrCoBi-based materials are notably higher than those of their n-type counterparts (fig. S6A). Because the inertial effective masses are comparable between the n- and p-type ZrCoBi (Fig. 3B), the carrier mobility of the p-type ZrCoBi-based materials remains similar to that of their n-type counterparts (fig. S6B). To further reveal the effect of electronic structure on the thermoelectric properties, we calculated the product of carrier concentration and the square of Seebeck coefficient (S^2n) for ZrCoBi-based materials, as shown in Fig. 4D. It can be observed that

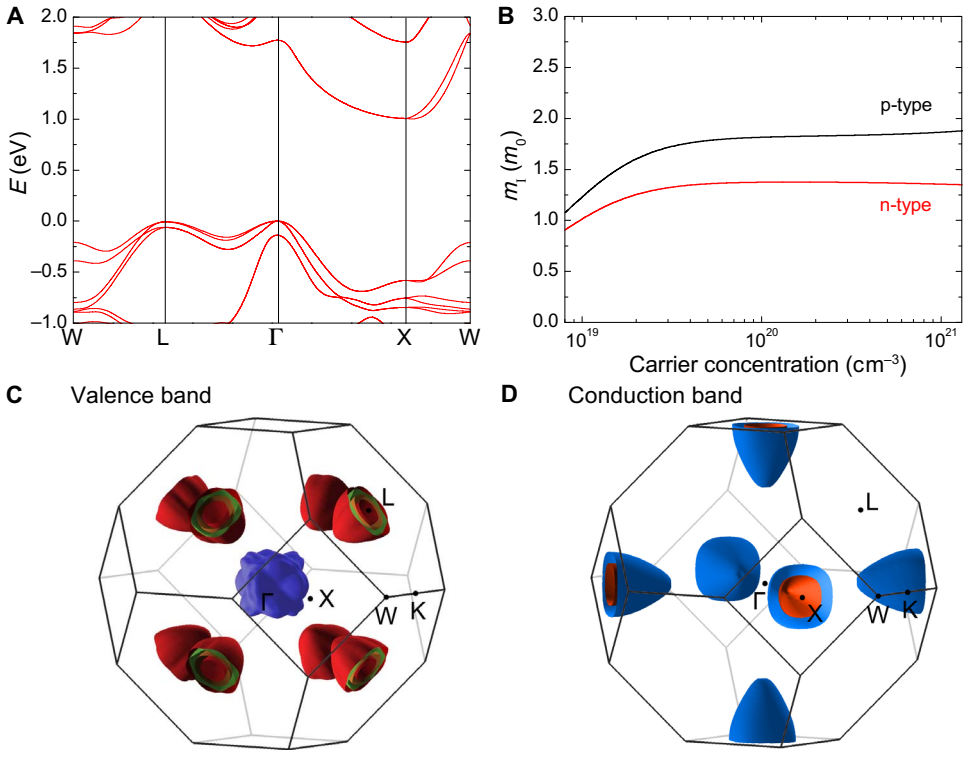

Fig. 3. Calculated electronic structure of ZrCoBi. (**A**) Band structure. (**B**) Calculated inertial effective mass for n- and p-type ZrCoBi at 1000 K. (**C**) Valence band carrier pockets. (**D**) Conduction band carrier pockets.

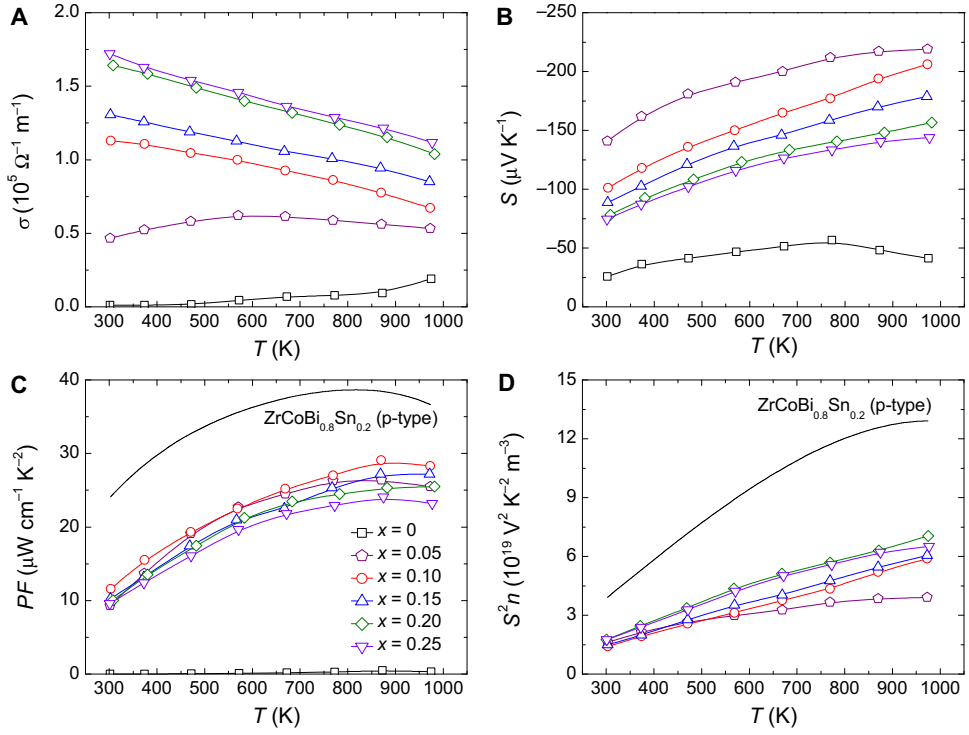

Fig. 4. Electronic properties for the n-type ZrCoBi-based half-Heuslers. (**A**) Electrical conductivity, (**B**) Seebeck coefficient, (**C**) power factor (*PF*), and (**D**) S^2n of $ZrCo_{1-x}Ni_xBi$.

the S^2n value of the p-type $ZrCoBi_{0.8}Sn_{0.2}$ is substantially higher than that of its n-type counterparts over the whole temperature range.

Thermal conductivity of the n-type ZrCoBi

Thermal conductivity of the n-type ZrCoBi-based half-Heuslers is shown in Fig. 5. The room temperature thermal conductivity of $ZrCo_{1-x}Ni_xBi$ is reduced considerably with the increase of Ni concentration (Fig. 5A). The room temperature thermal conductivity of the undoped ZrCoBi is ~8.9 W m^{-1} K^{-1}, and it is only ~4.3 W m^{-1} K^{-1} for $ZrCo_{0.75}Ni_{0.25}Bi$, a reduction of ~52%. This can be attributed to the high concentration of substitutional point defects (i.e., Ni at the Co site) that disrupt the phonon propagation. To reveal the phonon scattering effect by Ni doping, we further calculated the lattice thermal conductivity, as shown in Fig. 5B. The room temperature lattice thermal conductivity is ~8.9 W m^{-1} K^{-1} for the pristine ZrCoBi, and it is ~3.4 W m^{-1} K^{-1} for $ZrCo_{0.75}Ni_{0.25}Bi$, a reduction of ~62%. In addition to the Ni doping, thermal conductivity can also be largely reduced by alloying ZrCoBi with ZrCoSb (fig. S7). Compared to the heavy Ni doping that leads to the inferior power factor (Fig. 4C), alloying ZrCoBi with ZrCoSb can effectively reduce the thermal conductivity while maintaining a relatively high power factor (fig. S7C).

ZT and conversion efficiency of the n-type ZrCoBi

The dimensionless thermoelectric figure of merit *ZT* of the n-type $ZrCo_{1-x}Ni_xBi$ is shown in Fig. 6A. Evidently, Ni doping can effectively enhance the *ZT* and a peak *ZT* of ~0.74 can be achieved by $ZrCo_{0.9}Ni_{0.1}Bi$ at 973 K. By further alloying $ZrCo_{0.9}Ni_{0.1}Bi$ with ZrCoSb, the thermoelectric performance can be further improved (fig. S7F), and a reasonably high peak *ZT* of ~1 at 973 K can be obtained by $ZrCo_{0.9}Ni_{0.1}Bi_{0.85}Sb_{0.15}$. To demonstrate the reproducibility of this result, we prepared four different batches of $ZrCo_{0.9}Ni_{0.1}Bi_{0.85}Sb_{0.15}$. The measured thermoelectric properties are similar between the different batches, and the *ZT*s are quite comparable (fig. S8). To demonstrate the asymmetrical thermoelectric performance of the ZrCoBi-based materials, we also plotted the *ZT* of p-type $ZrCoBi_{0.65}Sb_{0.15}Sn_{0.2}$ (black solid line) in Fig. 6A for comparison. It should be noted that the thermoelectric performance of the p-type $ZrCoBi_{0.65}Sb_{0.15}Sn_{0.2}$ is noticeably better than that of the n-type $ZrCo_{0.9}Ni_{0.1}Bi_{0.85}Sb_{0.15}$ over the whole temperature range, which is in good agreement with our prediction (Fig. 2B). In addition, comparison of $ZrCo_{0.9}Ni_{0.1}Bi_{0.85}Sb_{0.15}$ with other state-of-the-art n-type half-Heusler materials is also made, as shown in Fig. 6B. Although the ZrNiSn-based materials show a higher *ZT* in the lower temperature range, their *ZT* is reduced at elevated temperature due to the bipolar effect. In contrast, the *ZT* of $ZrCo_{0.9}Ni_{0.1}Bi_{0.85}Sb_{0.15}$ increases monotonically within the studied temperature range, and therefore, $ZrCo_{0.9}Ni_{0.1}Bi_{0.85}Sb_{0.15}$ is comparable with the ZrNiSn-based materials at elevated temperature. In addition, $ZrCo_{0.9}Ni_{0.1}Bi_{0.85}Sb_{0.15}$ shows noticeably better thermoelectric performance than all of the other n-type half-Heuslers, e.g., ZrCoSb-based (*44*, *45*) and NbCoSn-based materials (*46*), over the whole temperature range. It should be noted that the ZrCoBi-based compound can achieve *ZT* around unity at 973 K for both carrier types. This makes the ZrCoBi compound highly promising for mid- and high-temperature thermoelectric power generation. To evaluate the potential of ZrCoBi-based materials for thermoelectric application, we measured the heat-to-electricity conversion efficiency of the single-leg $ZrCo_{0.9}Ni_{0.1}Bi_{0.85}Sb_{0.15}$. A maximum efficiency of ~7.9% can be obtained at the cold-side temperature of ~303 K and at hot-side temperature of ~953 K (Fig. 6C). The reported conversion efficiency of p-type single-leg $ZrCoBi_{0.65}Sb_{0.15}Sn_{0.2}$ is plotted in Fig. 6C for comparison (*42*). A unicouple of n-type $ZrCo_{0.9}Ni_{0.1}Bi_{0.85}Sb_{0.15}$ and p-type $ZrCoBi_{0.65}Sb_{0.15}Sn_{0.2}$ was further prepared. The dimension of each leg was optimized by considering the differences in electrical resistivity and thermal conductivity between the materials. Our results showed that a maximum heat-to-electricity conversion efficiency for the unicouple can be as high as ~10% at the cold-side temperature of ~303 K and at the hot-side temperature of ~983 K (Fig. 6D).

DISCUSSION

We have identified the relationship between the asymmetrical thermoelectric performance and the weighted mobility ratio. The weighted mobility ratio depends on the difference in electronic structures and the different scattering of carriers. The thermal stability difference may also lead to the asymmetrical performance in real applications. For example, the low stability of the Fe-based p-type skutterudites is a major limitation for achieving high efficiency in skutterudite modules. The relationship between the asymmetrical thermoelectric performance and the weighted mobility ratio can be used to predict the thermoelectric performance of the materials. However, it should be pointed out that the realization of both n- and p-type of semiconductors heavily depends on the dopability, which relates to the solubility limit and the defect level (i.e., shallow level or deep level) of the dopants (*3*). In addition, identifying and controlling the intrinsic defects that pin the Fermi level will be equally important for realizing the ambipolar doping. Therefore, the prediction of thermoelectric performance of unreported materials via the weighted mobility ratio can be roughly considered as an upper limit.

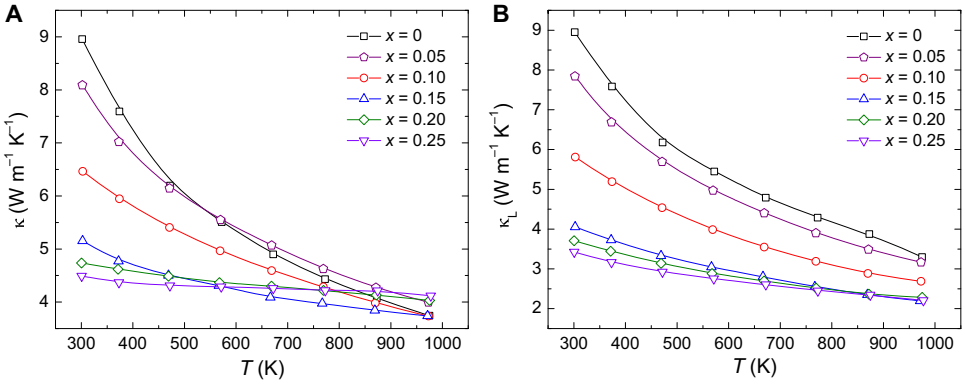

Fig. 5. Thermal conductivity of n-type ZrCoBi-based half-Heuslers. (**A**) Total thermal conductivity and (**B**) lattice thermal conductivity of $ZrCo_{1-x}Ni_xBi$.

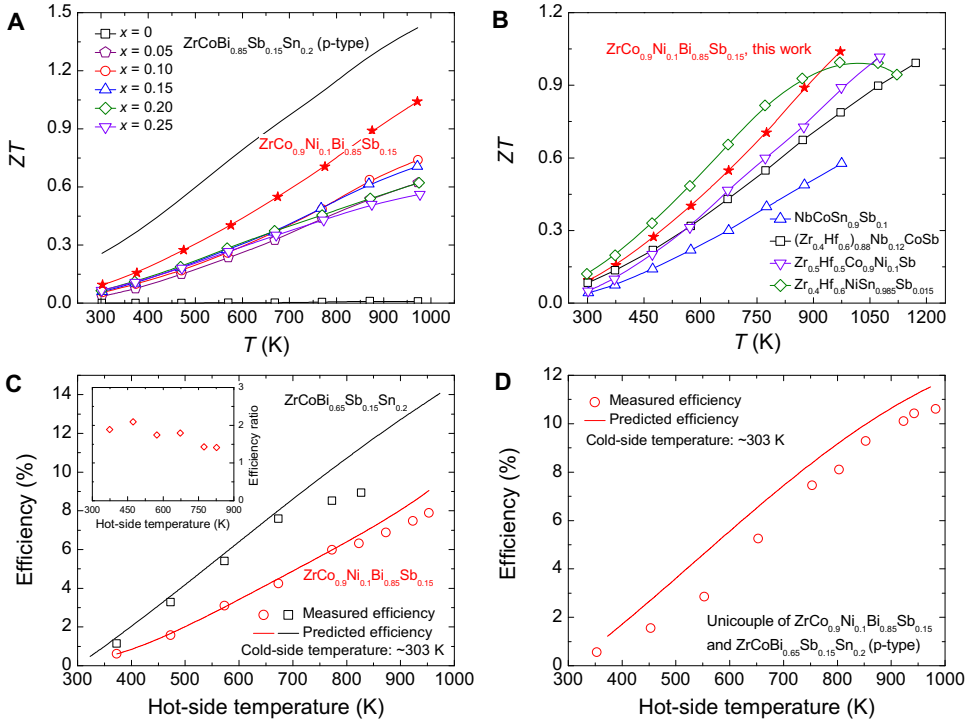

Fig. 6. Thermoelectric figure of merit of ZrCoBi-based half-Heuslers and measured heat-to-electricity conversion efficiency. (**A**) Thermoelectric figure of merit of $ZrCo_{1-x}Ni_xBi$ (n-type) and $ZrCo_{0.9}Ni_{0.1}Bi_{0.85}Sb_{0.15}$ (n-type) and (**B**) comparison of the *ZT*s between $ZrCo_{0.9}Ni_{0.1}Bi_{0.85}Sb_{0.15}$ (n-type) and the other state-of-the-art n-type half-Heuslers. Measured heat-to-electricity conversion efficiency for (**C**) single legs and (**D**) the unicouple of $ZrCo_{0.9}Ni_{0.1}Bi_{0.85}Sb_{0.15}$ (n-type) and $ZrCoBi_{0.65}Sb_{0.15}Sn_{0.2}$ (p-type). The inset in (C) is the ratio of the measured efficiency of p-type to n-type legs.

In this work, the thermoelectric performance of several materials has been predicted. Experimentally, we have prepared the n-type ZrCoBi-based half-Heuslers. By optimizing the carrier concentration and reducing the thermal conductivity, a peak *ZT* of ~1 at 973 K can be achieved for $ZrCo_{0.9}Ni_{0.1}Bi_{0.85}Sb_{0.15}$. Compared to the state-of-the-art n-type ZrNiSn-based half-Heuslers, the ZrCoBi-based materials demonstrate comparable thermoelectric performance at elevated temperature. In addition, the ZrCoBi-based materials outperform all of the other n-type half-Heuslers over the whole temperature range. The heat-to-electricity conversion efficiency is further measured for a unicouple consisting of the n- and p-type ZrCoBi-based materials. A maximum efficiency of ~10% can be obtained at the cold-side temperature of ~303 K and at the hot-side temperature of ~983 K. Our work demonstrates that the ZrCoBi-based half-Heuslers are quite promising for mid- and high-temperature thermoelectric power generation.

MATERIALS AND METHODS

Synthesis

n-type ZrCoBi-based half-Heuslers were prepared by the ball-milling and hot-pressing method. Zr sponge (99.2%; Alfa Aesar), Co powders (99.8%; Alfa Aesar), Bi ingots (99.999%; Alfa Aesar), Sb ingots (99.999%; Alfa Aesar), and Ni powders (99.8%; Alfa Aesar) according to the composition of $ZrCo_{1-x}Ni_xBi$ (x = 0, 0.05, 0.10, 0.15, 0.20, and 0.25) and $ZrCo_{0.9}Ni_{0.1}Bi_{1-y}Sb_y$ (y = 0, 0.10, 0.15, 0.20, and 0.30) were loaded into a stainless steel jar under an argon atmosphere in the glove box. The ball-milling process was conducted on an SPEX 8000M Mixer/Mill for 20 hours. It should be noted that, because of the cold-welding effect, large pieces can form and stick to the jar in the early stage of the ball-milling process. These pieces were carefully detached from the jar with a tool after the first 8 hours of ball milling. After 20 hours of ball milling, highly uniform and fine powders were obtained without any large pieces remaining in the jar. The obtained ball-milled powders (2.1 g) were loaded into the carbon die and compacted into a disc by a direct current–induced hot press at about 1173 K for 5 min and under pressure of ~80 MPa. The inner diameter of the carbon die is 12.7 mm, and the diameter of the carbon rods is 0.2 mm smaller.

Thermoelectric property measurement

The Seebeck coefficient and electrical conductivity were simultaneously obtained using a commercial system (ZEM-3, ULVAC) in helium atmosphere. The thermal conductivity $\kappa = DC_p\rho$ was calculated from the thermal diffusivity D (LFA 457, Netzsch), specific heat C_p (DSC 404 C, Netzsch), and mass density ρ (Archimedes' kit). Hall carrier concentrations (n_H) were measured on a commercial system (PPMS DynaCool, Quantum Design), with a magnetic field of ±3 T and an electrical current of 8 mA.

Heat-to-electricity conversion efficiency measurement

For the single-leg n-type $ZrCo_{0.9}Ni_{0.1}Bi_{0.85}Sb_{0.15}$, the thermoelectric materials were polished for a cross-section of 1.51 × 2.35 mm^2 and length of ~8.54 mm. For the unicouple of ZrCoBi-based materials, the dimensions are 1.51 × 2.35 × 8.54 mm^3 for the n-type $ZrCo_{0.9}Ni_{0.1}Bi_{0.85}Sb_{0.15}$ and 1.61 × 2.42 × 8.54 mm^3 for the p-type $ZrCoBi_{0.65}Sb_{0.15}Sn_{0.2}$. The cold-side temperature was maintained at ~303 K by water circulation. Because of the increasing of heat flow, the cold-side temperature will rise with the hot-side temperature. The difference between the measured efficiency and the predicted value increases with increasing hot-side

temperature because the predicted value is calculated on the basis of the fixed cold-side temperature (room temperature). The experiments were conducted under high vacuum (below 10^{-6} mbar) to reduce parasitic conduction and convection losses. To measure conversion efficiency (η), the input power from the hot side (Q_{in}) and the generated power (P) from the thermoelectric leg were measured at the same time. The direct measurement of Q_{in} is greatly challenging because of the heavy heat loss at high temperature. According to Fourier's law, a bulk polycrystalline graphite with measured geometry and thermal conductivity was placed below the cold-side end to measure the heat flow out of the cold-side end (Q_{out}). The thermal conductivity of the bulk polycrystalline graphite was confirmed by the method described above in the discussion on thermoelectric property measurements. To measure temperature differences of the leg and graphite bulk, K-type thermocouples were embedded at the interfaces. It should be noted that the hot-side temperature of graphite can be regarded as the cold-side temperature of the leg if the setup is working under a large pressure. The total Q_{in} equals the sum of Q_{out}, P, and radiation loss from the leg (Q_{rad}). Therefore, the conversion efficiency (η) can be written as follows

$$\eta = \frac{P}{Q_{in}} = \frac{P}{Q_{out} + P + Q_{rad}} \quad (4)$$

Because Q_{rad} cannot be directly measured, in real measurement, Q_{in} is composed of Q_{out} and P, which leads to the measurement error of η. By tuning the current in the circuit, a series of Q_{in}, P can be measured at the same time. Therefore, both maximum η and P can be found. The main sources of error in this system are the radiation heat, the rise of the cold-side temperature, the Seebeck coefficient of copper wire, and the parasitic electrical and heat loss. In the measurement of p-type leg efficiency (*42*), to offset the radiation loss, copper foil working as a radiation shield was brazed with copper plate at the hot side. Because this radiation shield is at a higher temperature than the leg, it will add additional heat flow into the leg so that the measured Q_{out} will actually be higher than without the shield. This should lead to a more conservative value of efficiency for the p-type leg, especially at high temperature.

Microstructural characterization

Phase compositions were characterized by x-ray diffraction on a PANalytical multipurpose diffractometer with an X'Celerator detector (PANalytical X'Pert Pro). The morphology and microstructures were characterized with a field-emission scanning electron microscope (FESEM, LEO 1525). Elemental mapping was conducted by energy-dispersive x-ray spectroscopy (JEOL JSM-6330F), as shown in fig. S9. Selected-area electron diffraction patterns and high-angle annular dark-field scanning transmission electron microscopy (HAADF-STEM) images were obtained with a JEM-ARM 200F TEM operated at 200 kV (fig. S10). The microscope was equipped with a cold FEG source and double-sextupole Cs correctors for STEM and TEM (for probe and imaging), respectively.

Theoretical calculations

Electronic structure and transport calculations were performed for the half-Heusler structure ZrCoBi based on density functional theory. For this purpose, the general potential linearized augmented planewave (LAPW) method as implemented in the WIEN2k code (*47*) was used. Spin-orbit, which is crucial, was included self-consistently for all states. The main results were obtained using the modified Becke Johnson (mBJ) potential and a lattice parameter of 6.186 Å. These calculations were done similarly to our previously reported electronic structure calculations for half-Heusler compounds (*42*, *48*). LAPW sphere radii of $R = 2.3$ bohr was used for all atoms. We used very well converged basis sets consisting of an LAPW sector determined by a cutoff, $RK_{max} = 9.0$, plus additional local orbitals, where K_{max} is the planewave sector cutoff. Transport integrals were performed with the BoltzTraP code and analyzed using the transM code to obtain inertial effective masses and an electronic fitness function for thermoelectric performance. The Brillouin zone sampling for the transport calculation was done using more than 40,000 points in the zone. Convergence of the Brillouin zone sampling was tested, as were the basis sets and other parameters. We also performed tests including the standard Perdew-Burke-Ernzerhof (PBE) generalized gradient approximation functional, as well as with the Vienna Ab initio Simulation Package (VASP) using the Heyd-Scuseria-Ernzerhof (HSE) screened hybrid functional. The main difference between the HSE and mBJ potential is in the band gap, which is enhanced from 1.0 eV with the mBJ potential to 1.2 eV in the HSE calculation.

SUPPLEMENTARY MATERIALS

Supplementary material for this article is available at http://advances.sciencemag.org/cgi/content/full/5/6/eaav5813/DC1

Section S1. Theoretical prediction of *ZT* value
Fig. S1. Theoretical prediction of *ZT* value.
Fig. S2. Thermoelectric properties of p-type NbCoSn-based and n-type TaFeSb-based materials.
Fig. S3. Phase composition of n-type ZrCoBi-based half-Heuslers.
Fig. S4. Microstructures of n-type ZrCoBi-based half-Heuslers.
Fig. S5. Room temperature Hall carrier concentration of $ZrCo_{1-x}Ni_xBi$.
Fig. S6. Comparison of the density-of-state effective mass and carrier mobility between n- and p-type ZrCoBi-based materials.
Fig. S7. Thermoelectric properties of $ZrCo_{0.9}Ni_{0.1}Bi_{1-y}Sb_y$ (y = 0, 0.10, 0.15, 0.20, and 0.30).
Fig. S8. Reproducibility of the thermoelectric performance of $ZrCo_{0.9}Ni_{0.1}Bi_{0.85}Sb_{0.15}$.
Fig. S9. Energy-dispersive spectroscopy mapping of $ZrCo_{0.9}Ni_{0.1}Bi_{0.85}Sb_{0.15}$.
Fig. S10. TEM images of $ZrCo_{0.9}Ni_{0.1}Bi_{0.85}Sb_{0.15}$.
Table S1. Transport data of state-of-the-art thermoelectric materials.

REFERENCES AND NOTES

1. L. E. Bell, Cooling, heating, generating power, and recovering waste heat with thermoelectric systems. *Science* **321**, 1457–1461 (2008).
2. W. Liu, J. Hu, S. Zhang, M. Deng, C. Han, Y. Liu, New trends, strategies and opportunities in thermoelectric materials: A perspective. *Mater. Today Phys.* **1**, 50–60 (2017).
3. J. Mao, Z. Liu, J. Zhou, H. Zhu, Q. Zhang, G. Chen, Z. Ren, Advances in thermoelectrics. *Adv. Phys.* **67**, 69–147 (2018).
4. G. J. Snyder, E. S. Toberer, Complex thermoelectric materials. *Nat. Mater.* **7**, 105–114 (2008).
5. H. Zhao, J. Sui, Z. Tang, Y. Lan, Q. Jie, D. Kraemer, K. McEnaney, A. Guloy, G. Chen, Z. Ren, High thermoelectric performance of MgAgSb-based materials. *Nano Energy* **7**, 97–103 (2014).
6. Z. Liu, Y. Wang, J. Mao, H. Geng, J. Shuai, Y. Wang, R. He, W. Cai, J. Sui, Z. Ren, Lithium doping to enhance thermoelectric performance of MgAgSb with weak electron-phonon coupling. *Adv. Energy Mater.* **6**, 1502269 (2016).
7. Z. Liu, J. Mao, J. Sui, Z. Ren, High thermoelectric performance of α-MgAgSb for power generation. *Energy Environ. Sci.* **11**, 23–44 (2018).
8. Q. Zhang, B. Liao, Y. Lan, K. Lukas, W. Liu, K. Esfarjani, C. Opeil, D. Broido, G. Chen, Z. Ren, High thermoelectric performance by resonant dopant indium in nanostructured SnTe. *Proc. Natl. Acad. Sci. U.S.A.* **110**, 13261–13266 (2013).
9. G. Tan, F. Shi, S. Hao, H. Chi, T. P. Bailey, L.-D. Zhao, C. Uher, C. Wolverton, V. P. Dravid, M. G. Kanatzidis, Valence band modification and high thermoelectric performance in SnTe heavily alloyed with MnTe. *J. Am. Chem. Soc.* **137**, 11507–11516 (2015).
10. Y. Gelbstein, J. Davidow, S. N. Girard, D. Y. Chung, M. Kanatzidis, Controlling metallurgical phase separation reactions of the $Ge_{0.87}Pb_{0.13}Te$ alloy for high thermoelectric performance. *Adv. Energy Mater.* **3**, 815–820 (2013).
11. J. Li, X. Zhang, Z. Chen, S. Lin, W. Li, J. Shen, I. T. Witting, A. Faghaninia, Y. Chen, A. Jain, L. Chen, G. J. Snyder, Y. Pei, Low-symmetry rhombohedral GeTe thermoelectrics. *Joule* **2**, 976–987 (2018).

12. Z. Liu, J. Sun, J. Mao, H. Zhu, W. Ren, J. Zhou, Z. Wang, D. J. Singh, J. Sui, C.-W. Chu, Z. Ren, Phase-transition temperature suppression to achieve cubic GeTe and high thermoelectric performance by Bi and Mn codoping. *Proc. Natl. Acad. Sci. U.S.A.* **115**, 5332–5337 (2018).
13. T. Caillat, J.-P. Fleurial, A. Borshchevsky, Preparation and thermoelectric properties of semiconducting Zn_4Sb_3. *J. Phys. Chem. Solids* **58**, 1119–1125 (1997).
14. G. S. Pomrehn, A. Zevalkink, W. G. Zeier, A. van de Walle, G. J. Snyder, Defect-controlled electronic properties in AZn_2Sb_2 Zintl phases. *Angew. Chem. Int. Ed.* **53**, 3422–3426 (2014).
15. W. Liu, X. Tan, K. Yin, H. Liu, X. Tang, J. Shi, Q. Zhang, C. Uher, Convergence of conduction bands as a means of enhancing thermoelectric performance of *n*-type $Mg_2Si_{1-x}Sn_x$ solid solutions. *Phys. Rev. Lett.* **108**, 166601 (2012).
16. Q. Zhang, L. Cheng, W. Liu, Y. Zheng, X. Su, H. Chi, H. Liu, Y. Yan, X. Tang, C. Uher, Low effective mass and carrier concentration optimization for high performance p-type $Mg_{2(1-x)}Li_{2x}Si_{0.3}Sn_{0.7}$ solid solutions. *Phys. Chem. Chem. Phys.* **16**, 23576–23583 (2014).
17. J. Mao, H. S. Kim, J. Shuai, Z. Liu, R. He, U. Saparamadu, F. Tian, W. Liu, Z. Ren, Thermoelectric properties of materials near the band crossing line in Mg_2Sn-Mg_2Ge-Mg_2Si system. *Acta Mater.* **103**, 633–642 (2016).
18. W. Liu, H. S. Kim, S. Chen, Q. Jie, B. Lv, M. Yao, Z. Ren, C. P. Opeil, S. Wilson, C.-W. Chu, Z. Ren, n-type thermoelectric material $Mg_2Sn_{0.75}Ge_{0.25}$ for high power generation. *Proc. Natl. Acad. Sci. U.S.A.* **112**, 3269–3274 (2015).
19. H. Tamaki, H. K. Sato, T. Kanno, Isotropic conduction network and defect chemistry in $Mg_{3+\delta}Sb_2$-based layered Zintl compounds with high thermoelectric performance. *Adv. Mater.* **28**, 10182–10187 (2016).
20. J. Zhang, L. Song, S. H. Pedersen, H. Yin, L. T. Hung, B. B. Iversen, Discovery of high-performance low-cost n-type Mg_3Sb_2-based thermoelectric materials with multi-valley conduction bands. *Nat. Commun.* **8**, 13901 (2017).
21. J. Mao, J. Shuai, S. Song, Y. Wu, R. Dally, J. Zhou, Z. Liu, J. Sun, Q. Zhang, C. dela Cruz, S. Wilson, Y. Pei, D. J. Singh, G. Chen, C.-W. Chu, Z. Ren, Manipulation of ionized impurity scattering for achieving high thermoelectric performance in n-type Mg_3Sb_2-based materials. *Proc. Natl. Acad. Sci. U.S.A.* **114**, 10548–10553 (2017).
22. J. Mao, Y. Wu, S. Song, Q. Zhu, J. Shuai, Z. Liu, Y. Pei, Z. Ren, Defect engineering for realizing high thermoelectric performance in n-type Mg_3Sb_2-based materials. *ACS Energy Lett.* **2**, 2245–2250 (2017).
23. C. Yu, T. Zhu, R. Shi, Y. Zhang, X. Zhao, J. He, High-performance half-Heusler thermoelectric materials $Hf_{1-x}Zr_xNiSn_{1-y}Sb_y$ prepared by levitation melting and spark plasma sintering. *Acta Mater.* **57**, 2757–2764 (2009).
24. S. Chen, K. C. Lukas, W. Liu, C. P. Opeil, G. Chen, Z. Ren, Effect of Hf concentration on thermoelectric properties of nanostructured n-type half-Heusler materials $Hf_xZr_{1-x}NiSn_{0.99}Sb_{0.01}$. *Adv. Energy Mater.* **3**, 1210–1214 (2013).
25. C. Fu, S. Bai, Y. Liu, Y. Tang, L. Chen, X. Zhao, T. Zhu, Realizing high figure of merit in heavy-band *p*-type half-Heusler thermoelectric materials. *Nat. Commun.* **6**, 8144 (2015).
26. R. He, D. Kraemer, J. Mao, L. Zeng, Q. Jie, Y. Lan, C. Li, J. Shuai, H. S. Kim, Y. Liu, D. Broido, C.-W. Chu, G. Chen, Z. Ren, Achieving high power factor and output power density in p-type half-Heuslers $Nb_{1-x}Ti_xFeSb$. *Proc. Natl. Acad. Sci. U.S.A.* **113**, 13576–13581 (2016).
27. J. Shen, L. Fan, C. Hu, T. Zhu, J. Xin, T. Fu, D. Zhao, X. Zhao, Enhanced thermoelectric performance in the n-type NbFeSb half-Heusler compound with heavy element Ir doping. *Mater. Today Phys.* **8**, 62–70 (2019).
28. B. Poudel, Q. Hao, Y. Ma, Y. Lan, A. Minnich, B. Yu, X. Yan, D. Wang, A. Muto, D. Vashaee, X. Chen, J. Liu, M. S. Dresselhaus, G. Chen, Z. Ren, High-thermoelectric performance of nanostructured bismuth antimony telluride bulk alloys. *Science* **320**, 634–638 (2008).
29. L. Hu, T. Zhu, X. Liu, X. Zhao, Point defect engineering of high-performance bismuth-telluride-based thermoelectric materials. *Adv. Funct. Mater.* **24**, 5211–5218 (2014).
30. Y. Pei, X. Shi, A. LaLonde, H. Wang, L. Chen, G. J. Snyder, Convergence of electronic bands for high performance bulk thermoelectrics. *Nature* **473**, 66–69 (2011).
31. Y. Pei, A. D. LaLonde, N. A. Heinz, X. Shi, S. Iwanaga, H. Wang, L. Chen, G. J. Snyder, Stabilizing the optimal carrier concentration for high thermoelectric efficiency. *Adv. Mater.* **23**, 5674–5678 (2011).
32. Y. Pei, A. D. LaLonde, H. Wang, G. J. Snyder, Low effective mass leading to high thermoelectric performance. *Energy Environ. Sci.* **5**, 7963–7969 (2012).
33. H. Wang, Y. Pei, A. D. LaLonde, G. J. Snyder, Weak electron-phonon coupling contributing to high thermoelectric performance in n-type PbSe. *Proc. Natl. Acad. Sci. U.S.A.* **109**, 9705–9709 (2012).
34. L.-D. Zhao, J. He, C.-I. Wu, T. P. Hogan, X. Zhou, C. Uher, V. P. Dravid, M. G. Kanatzidis, Thermoelectrics with earth abundant elements: High performance p-type PbS nanostructured with SrS and CaS. *J. Am. Chem. Soc.* **134**, 7902–7912 (2012).
35. Q. Zhang, Q. Song, X. Wang, J. Sun, Q. Zhu, K. Dahal, X. Lin, F. Cao, J. Zhou, S. Chen, G. Chen, J. Mao, Z. Ren, Deep defect level engineering: A strategy of optimizing the carrier concentration for high thermoelectric performance. *Energy Environ. Sci.* **11**, 933–940 (2018).
36. B. C. Sales, D. Mandrus, R. K. Williams, Filled skutterudite antimonides: A new class of thermoelectric materials. *Science* **272**, 1325–1328 (1996).
37. X. Shi, J. Yang, J. R. Salvador, M. Chi, J. Y. Cho, H. Wang, S. Bai, J. Yang, W. Zhang, L. Chen, Multiple-filled skutterudites: High thermoelectric figure of merit through separately optimizing electrical and thermal transports. *J. Am. Chem. Soc.* **133**, 7837–7846 (2011).
38. G. Joshi, H. Lee, Y. Lan, X. Wang, G. Zhu, D. Wang, R. W. Gould, D. C. Cuff, M. Y. Tang, M. S. Dresselhaus, G. Chen, Z. Ren, Enhanced thermoelectric figure-of-merit in nanostructured p-type silicon germanium bulk alloys. *Nano Lett.* **8**, 4670–4674 (2008).
39. X. Wang, H. Lee, Y. Lan, G. Zhu, G. Joshi, D. Wang, J. Yang, A. J. Muto, M. Tang, J. Klatsky, S. Song, M. S. Dresselhaus, G. Chen, Z. Ren, Enhanced thermoelectric figure of merit in nanostructured *n*-type silicon germanium bulk alloy. *Appl. Phys. Lett.* **93**, 193121 (2008).
40. R. P. Chasmar, R. Stratton, The thermoelectric figure of merit and its relation to thermoelectric generators. *Int. J. Electron.* **7**, 52–72 (1959).
41. H. Wang, Y. Pei, A. D. LaLonde, G. J. Snyder, in *Thermoelectric Nanomaterials*, K. Koumoto, T. Mori, Eds. (Springer, 2013), pp. 3–32.
42. H. Zhu, R. He, J. Mao, Q. Zhu, C. Li, J. Sun, W. Ren, Y. Wang, Z. Liu, Z. Tang, A. Sotnikov, Z. Wang, D. Broido, D. J. Singh, G. Chen, K. Nielsch, Z. Ren, Discovery of ZrCoBi-based half-Heuslers with high thermoelectric conversion efficiency. *Nat. Commun.* **9**, 2497 (2018).
43. G. Xing, J. Sun, Y. Li, X. Fan, W. Zheng, D. J. Singh, Electronic fitness function for screening semiconductors as thermoelectric materials. *Phys. Rev. Mater.* **1**, 065405 (2017).
44. R. He, H. Zhu, J. Sun, J. Mao, H. Reith, S. Chen, G. Schierning, K. Nielsch, Z. Ren, Improved thermoelectric performance of n-type half-Heusler $MCo_{1-x}Ni_xSb$ (M = Hf, Zr). *Mater. Today Phys.* **1**, 24–30 (2017).
45. Y. Liu, C. Fu, K. Xia, J. Yu, X. Zhao, H. Pan, C. Felser, T. Zhu, Lanthanide contraction as a design factor for high performance half-Heusler thermoelectric materials. *Adv. Mater.* **30**, 1800881 (2018).
46. R. He, L. Huang, Y. Wang, G. Samsonidze, B. Kozinsky, Q. Zhang, Z. Ren, Enhanced thermoelectric properties of n-type NbCoSn half-Heusler by improving phase purity. *APL Mater.* **4**, 104804 (2016).
47. K. Schwarz, P. Blaha, G. K. H. Madsen, Electronic structure calculations of solids using the WIEN2k package for material sciences. *Comput. Phys. Commun.* **147**, 71–76 (2002).
48. H. Zhu, J. Mao, Y. Li, J. Sun, Y. Wang, Q. Zhu, G. Li, Q. Song, J. Zhou, Y. Fu, R. He, T. Tong, Z. Liu, W. Ren, L. You, Z. Wang, J. Luo, A. Sotnikov, J. Bao, K. Nielsch, G. Chen, D. J. Singh, Z. Ren, Discovery of TaFeSb-based half-Heuslers with high thermoelectric performance. *Nat. Commun.* **10**, 270 (2019).

Acknowledgments: We thank Y. Li, G. Xing, C. Chen, Q. Zhang, and R. He for their help in theoretical calculations and experiments. **Funding:** Theoretical work at the University of Missouri was supported by the U.S. Department of Energy, Office of Basic Energy Science, under award number DE-SC0019114. Y.W. acknowledges the National Natural Science Foundation of China (grant no.11474329). **Author contributions:** H.Z., J.M., and Z.R. designed the research; H.Z. and J.M. performed experimental research; D.J.S., J.S., and Z.F. performed the theoretical calculations; H.Z. and Q.Z. measured the efficiency; Y.W. conducted the TEM characterization; Z.L. contributed analytical tools; H.Z., J.M., D.J.S., and Z.R. prepared the manuscript; and all authors commented on the manuscript. **Competing interests:** The authors declare that they have no competing interests. **Data and materials availability:** All data needed to evaluate the conclusions in the paper are present in the paper and/or the Supplementary Materials. Additional data related to this paper may be requested from the authors.

Submitted 30 September 2018
Accepted 15 May 2019
Published 21 June 2019
10.1126/sciadv.aav5813

Citation: H. Zhu, J. Mao, Z. Feng, J. Sun, Q. Zhu, Z. Liu, D. J. Singh, Y. Wang, Z. Ren, Understanding the asymmetrical thermoelectric performance for discovering promising thermoelectric materials. *Sci. Adv.* **5**, eaav5813 (2019).

Understanding the asymmetrical thermoelectric performance for discovering promising thermoelectric materials

Hangtian Zhu, Jun Mao, Zhenzhen Feng, Jifeng Sun, Qing Zhu, Zihang Liu, David J. Singh, Yumei Wang and Zhifeng Ren

Sci Adv **5** (6), eaav5813.
DOI: 10.1126/sciadv.aav5813